Article

Degradation of Pyraclostrobin in Water Using a Novel Hybrid Gas–Liquid Phase Discharge Reactor

Hongwei Shen [1,2,3], Hao Yuan [2], Jianping Liang [2], Xiongfeng Zhou [2], Pingji Ge [1,3], Yang Liu [1,2,3], Tian Gao [1,2,3], Kun Yang [1,3,*] and Dezheng Yang [1,2,*]

1. School of Sciences, Shihezi University, Shihezi 832003, China
2. Key Laboratory of Materials Modification by Laser, Ion, and Electron Beams, Dalian University of Technology, Ministry of Education, Dalian 116024, China
3. Xinjiang Production & Construction Corps Key Laboratory of Advanced Energy Storage Materials and Technology, Shihezi University, Shihezi 832000, China
* Correspondence: yangk_shz@sina.com (K.Y.); yangdz@dlut.edu.cn (D.Y.)

Abstract: In this paper, the hybrid gas–liquid discharge plasma can efficiently degrade pesticide residues in water driven by nanosecond pulse power, which can achieve the simultaneous discharge process in the liquid and gas phases. The relevant factors are systematically investigated, including the waveforms of discharge current and pulse voltage, discharge images, and optical emission spectra during the discharge process. The Stark broadening of H_α calculates the electron density. The effects of the pulse peak voltage and discharge time on the emission intensities of OH ($A^2\sum \to X^2\prod$), N_2 ($C^3\prod_u \to B^3\prod_g$), H_α, and O ($3p^5P \to 3s^5S^0$) are discussed in-depth by the optical emission spectra. The gas–liquid discharge plasma with an electron density of 7.14×10^{17} cm^{-3} was found. The emission intensities of OH ($A^2\sum \to X^2\prod$), N_2 ($C^3\prod_u \to B^3\prod_g$), H_α, and O ($3p^5P \to 3s^5S^0$) present the rising trend by increasing the pulse peak voltage and discharge time. In addition, pyraclostrobin is adopted as the research object to study the removal efficiency of pollutants. The results confirm that pyraclostrobin can be completely degraded after 10 min of plasma treatment with the pulse peak voltage of 28 kV, and the degradation rate and energy yield was 0.323 min^{-1}, and 1.91 g/kWh, respectively. The intermediate products and the possible degradation mechanism of pyraclostrobin are further explored by combining the results of high-performance liquid chromatography–mass spectrometry (HPLC-MS/MS) and density functional theory (DFT), the developmental toxicity of the intermediate products was analyzed, which provided a scheme for the treatment of pesticide wastewater by gas–liquid discharge plasma technology.

Keywords: nonthermal plasma; degradation; gas–liquid discharge; electron density

1. Introduction

In recent years, nanosecond pulsed discharge plasma (NPDP) technology has been proven to be an effective way to remove toxic and harmful substances from wastewater, such as pesticides, antibiotics, heavy metals, and persistent organic pollutants [1–5]. Compared with the common methods like adsorption, chemical precipitation, and bioremediation for wastewater treatment, NPDP technology presents the unique advantages of simple equipment, high degradation efficiency, environmental friendliness, and no requirement for subsequent processing, which makes it our current research focus.

In the process of NPDP, numerous reactive species are generated to promote the generation and propagation of plasma physical and chemical reactions. High-energy electrons, H_2O_2, OH, O_3, reactive oxygen and nitrogen species (RONS) play a leading role in the degradation of organic matter. The reactive species dissolve/diffuse into the liquid and then react with organic pollutants in the water body to mineralize and degrade the pollutants [5–9]. Wang et al. studied the degradation of tetracycline in water with a transient spark gas–liquid discharge. The results showed that the removal rate of tetracycline reaches

90.2% after 10 min. Furthermore, experiment on seed germination and plant growth were carried out in the treated water, and the results proved that it was feasible to use treated water to promote crop growth [10]. Zhang et al. adopted dielectric barrier discharge (DBD) to remove bacterial endotoxin. The removal efficiency of total endotoxin activity was up to 92% after 180 s of plasma treatment, which was more than that of previously reported methods [11–14]. Wang et al. used dielectric barrier discharge (DBD) plasma to degrade carbendazim (MBC) in an aqueous solution. After 10 min of discharge treatment, the degradation rate of MBC reached 98.04%, and the biotoxicity of MBC degradation products after DBD plasma treatment was significantly reduced [15]. Fang et al. used non-thermal plasma (NTP) to remove methyl parathion from water. In the He atmosphere, the removal rate can reach 90% after 2 min, and OH is the primary degradation factor. Toxicity assessment software (T.E.S.T.) was used to test the intermediates, and the intermediate biotoxicity was reduced [16]. Zhang et al. reported that plasma discharge with injected bubbles was more effective than a plasma discharge system alone in removing cefixime antibiotics in water [17].

Recently, researchers have devoted themselves to developing different types of discharge setups to obtain optimized discharge structures better suited for practice application [9,18]. The main types of gas–liquid discharge include discharge plasma above the water surface [19,20], discharge plasma in direct contact with or in water [21], and discharge plasma injected with bubbles below water [22–24]. When the discharge plasma is not in contact with the water, the discharge with the low breakdown voltage will be higher than the liquid and not in connection with the liquid, and the gaseous highly reactive species produced by the discharge plasma will enter the water to play a critical role [25]. When the discharge plasma comes into direct contact with liquid or discharges in liquid, its complete contact with the liquid phase is conducive to the generation and action of short-lived reactive species (OH and O) [26,27]. Bubble discharge plasma adopts the high-pressure needle electrode to enter into the bubble. The formation of bubbles effectively increases the reaction surface area and promotes the mass transfer process of gaseous reactants to the liquid phase [28].

In this study, A novel hybrid gas–liquid discharge plasma reactor was rationally designed to generate underwater bubble discharge plasma and gas discharge plasma above the water surface. The nanosecond pulsed power was used to drive the gas–liquid discharge process with the needle array gas–liquid discharge reactor to degrade pyraclostrobin (PYR, Chemical formula: $C_{19}H_{18}ClN_3O_4$) in water. The ability of the gas–liquid discharge to generate reactive species and the removal efficiency of PYR was emphatically investigated. The plasma electron density of the discharge was qualitatively measured by the Stark broadening of Hα. In addition, the possible degradation mechanism of PYR was validated based on the degradation intermediates detected by HPLC-MS/MS and the result of DFT, the toxicity evaluation software tool (T.E.S.T.) was used to predict and evaluate the toxicity of PYR and intermediate products.

2. Materials and Methods

2.1. Experimental Setup

The schematic diagram of the experimental setup is displayed in Figure 1, which consisted of a nanosecond pulsed gas–liquid discharge (NPG-LD) plasma reactor, a nanosecond pulsed power, an optical diagnosis system, and an electrical measurement system. The discharge reactor comprised a quartz tube with an inner diameter of about 34 mm, eight hollow stainless steel needle electrodes, and a Teflon chamber. The quartz tube containing 15 mL of solution was fixed on the Teflon chamber. Seven needle electrodes fixed in a Teflon chamber served as the high-voltage (HV) electrodes, which were further connected to a bipolar nanosecond pulsed generator (DGM-40, Dalian Power Supply Technology Co. Ltd., Dalian, China). One stainless steel needle was fixed in the Teflon chamber and acted as the ground electrode above the quartz tube. The 0.4 mm thick polyethylene tubes were nested within the HV needle electrodes and worked as the dielectric barrier. The working gas (air)

entered the reactor through HV needle electrodes, and mass flow controllers controlled the gas flow. The pulse voltage and discharge current of the NPG-LD were measured by a digital oscilloscope (Tektronix MDO3034, 350 MHz, Tektronix Inc., Shanghai, China) equipped with a 1:1000 high-voltage probe (Tektronix P6015A, 3.0 pF, 100 MΩ) and a current probe (Tektronix TCP312, 100 MHz, Tektronix Inc., Shanghai, China). The optical fiber was fixed on a 3D displacement platform that can be adjusted vertically and horizontally. Spectral diagnostics is performed using optical emission spectroscopy of a spectrometer (Andor SR-750i, grating groove of 2400 lines/mm, blazed wavelength of 200 nm, Oxford Instruments., Shanghai, China).
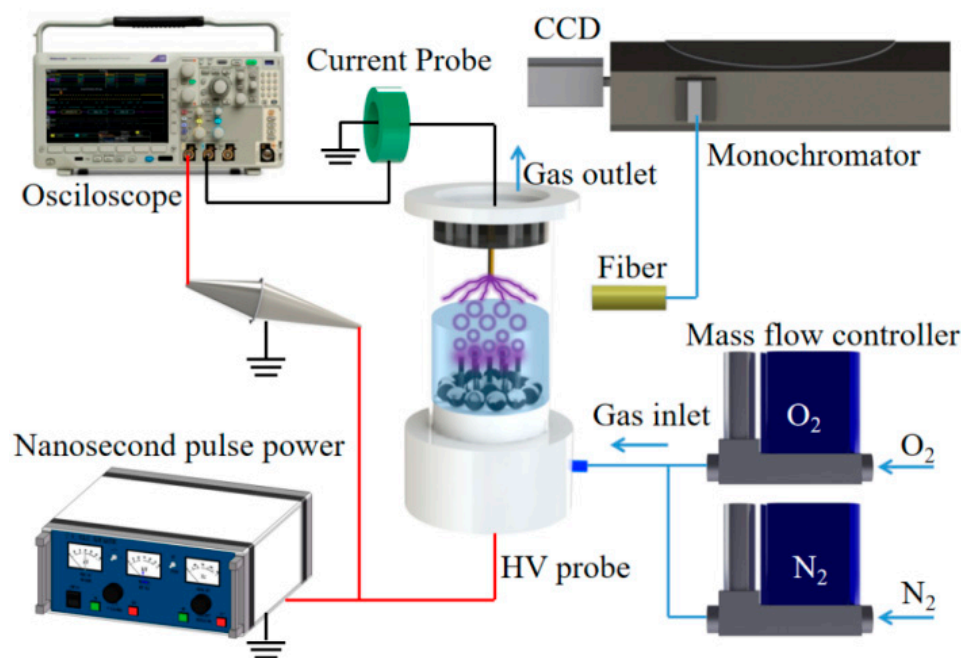
Figure 1. Schematic diagram of the experimental setup for PYR degradation in an NPG-LD reactor.

2.2. Materials and Analytical Methods

The PYR is purchased from the North Weiye Institute of Metrology Technology (Beijing, China). HPLC-grade acetonitrile is obtained from Spectrum Chemical Mfg. Ethanol (Et-OH) and other chemical reagents with analytical grades are obtained from Bo-Nuo Chemical Reagent Co. Ltd. (Dalian, China). The corresponding solution used is prepared with deionized water in the experiment.

The PYR concentrations were measured by a UV-vis spectrophotometer (Agilent Cary 5000, Agilent Technology Inc., Santa Clara, CA, USA) with a calibrated wavelength of 276 nm. The PYR removal efficiency η (%) was calculated by Equation (1) [29].

$$\eta = \left(1 - \frac{C_t}{C_0}\right) \times 100\%, \tag{1}$$

The pseudo first-order kinetic model is used to analyze the dynamic of PYR degradation Equation (2) [30]:

$$\ln \frac{C_t}{C_0} = -k\,t, \tag{2}$$

where η represents the PYR removal efficiency, C_0 is the initial concentration of untreated PYR (20 mg/L), C_t is the concentration of PYR at the arbitrary treatment time, and k is the pseudo-first-order kinetic constant (min^{-1}).

The discharge power P was calculated by Equation (3) [6].

$$P = f \int_0^t i(t)\, u(t)\, dt, \tag{3}$$

where f indicates the pulsed repetition rate, $i(t)$ represents the instantaneous discharge current, and $u(t)$ is the pulse peak voltage.

The energy yield (EY) of PYR removal was calculated using Equation (4) [31].

$$EY\ (\text{g/kWh}) = \frac{6 \times 10^{-2}\, C_0 \times V \times \eta}{P\, t}, \tag{4}$$

where P is the discharge power (W), and V is solution volume (mL).

The intermediate products of the PYR degradation process were identified using HPLC-MS/MS (Agilent RRLC/6410B, Agilent Technologies Inc., Santa Clara, CA, USA) equipped with a C18 column (2.1 × 100 mm, 3.5 μm). The C18 column temperature is set at 40 °C. The injection volume was 10 μL. The mobile phase consisted of deionized water (A) and acetonitrile (B) with gradient elution at a 0.25 mL/min flow rate as follows: 0–10 min, 80% B; 10–15 min, 80% B; 15.1–22 min, 10% B. The electrospray ionization (ESI) source was operated in positive ion mode, and the ionization voltage was set at 4 kV. The gas temperature and flow rates were 350 °C and 8 L/min, respectively.

3. Results and Discussion

3.1. Discharge Characteristics of NPG-LD

Figure 2 shows the discharge image of the NPG-LD reactor at a pulse repetition rate of 150 Hz and a pulse peak voltage of 24 kV by a nanosecond pulsed power supply, which was captured by a digital camera. The seven HV needle electrodes located in the lower part of the reactor presented dispersive discharges, and the plasma luminescence intensity was weak with a lavender color. Among them, the needle electrodes in the central part exhibited weak discharges. The ground electrode at the upper part of the reactor demonstrated a streamer discharge, which was accompanied by relatively strong light intensity. In addition, the plasma generated at the ground electrode was in complete contact with the bubble burst area. The discharge current and pulse voltage waveforms are recorded using an oscilloscope to further explore the effects of the pulse peak voltages on the discharge mode transition and discharge characteristics.
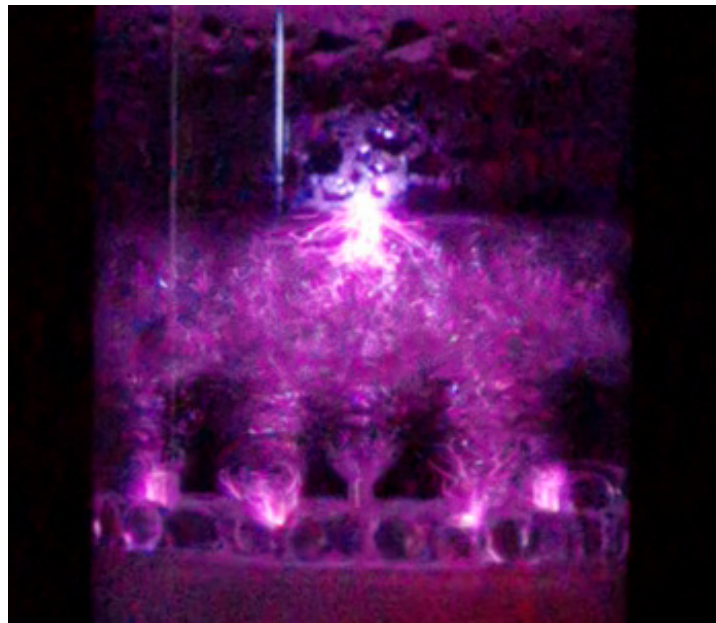
Figure 2. Discharge image of the NPG-LD under 24 kV of pulse peak voltage with a 150 Hz Pulse repetition rate.

Figure 3 displays the corresponding waveforms under different pulse peak voltages and discharge currents when the pulse repetition rate was set to 150 Hz. When the pulse peak voltage is lower than 24 kV, there is only one discharge current peak per half-pulse period (positive pulse half-cycle or negative pulse half-cycle). When the pulse peak voltage exceeds 24 kV, two discharge current peaks appear per half-pulse cycle. Figure 3a exhibits the waveforms of the pulse voltage and discharge current at the pulse peak voltage of 20 kV. When the discharge current is set to 1.79 A, and the duration time of 45 ns, the average power can reach 0.31 W. When the pulse peak voltage is 28 kV, two major discharge current peaks appear in every half-pulsed cycle. Figure 3b displays the waveforms of the pulse voltage and discharge current. The discharge current of the first current peak is 3.41 A with the duration time of 60 ns, and the average power is calculated to be 0.76 W. The discharge current of the second current peak corresponds to 3.25 A, the discharge duration time is approximately 500 ns, and the discharge power reaches the highest value of 4.21 W. Similar results were also characterized by the short spark discharge, as reported by Wang et al. [32] Compared with other gas–liquid discharge forms, this technology possesses the unique advantages of high electron density, rich reactive species, and low temperature.
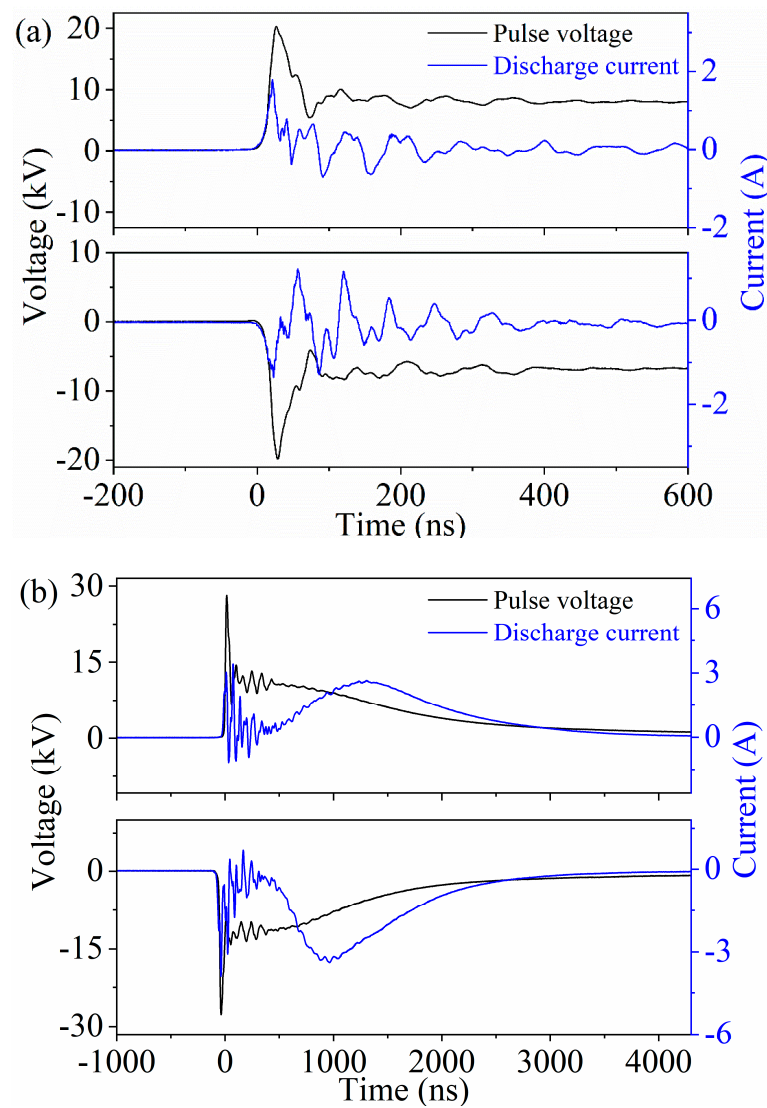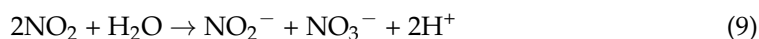
Figure 3. Waveforms of the pulse voltage and discharge current at (**a**) 20 kV and (**b**) 28 kV with a 150 Hz pulse repetition rate.
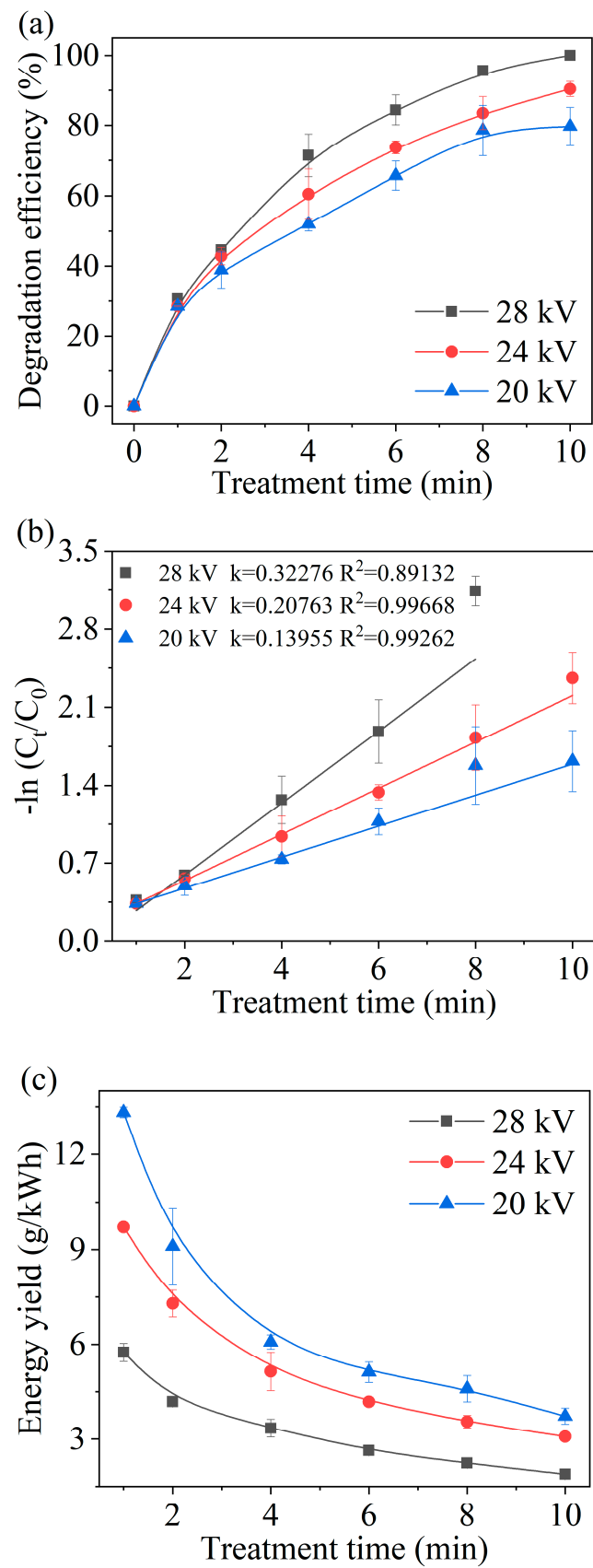
3.2. Effect of Pulse Peak Voltage on the Removal Efficiency of PYR

The removal efficiency of PYR in water varied with the treatment at different pulse peak voltages, as shown in Figure 4a. The degradation efficiency of PYR was greatly improved with increasing pulse peak voltage and discharge treatment time. After 10 min of treatment, the degradation efficiency of PYR increased from 79.7% to 100% when the pulse peak voltage changed from 20 kV to 28 kV, which was due to the increase of energy input caused by the conversion of discharge mode. The discharge mode at the cathode changed from streamer discharge to streamer-instantaneous spark discharge. The rapid conduction between the two electrodes produced more reactive species and high-energy electrons. The excitation, ionization, and dissociation reactions in the discharge process generated more reactive species to oxidize PYR. In addition, the degradation rate of PYR increased rapidly at the beginning of plasma treatment but then rose slowly. There were two reasons: the NO_3^- and NO_2^- (Equations (5)–(9)) produced by gas–liquid discharge led to a decrease in the pH of the solution, and the degradation of PYR under acidic conditions had an inhibitory effect [33–35]; these intermediate products consumed more reactive species [36]. Table 1 shows the degradation efficiency of PYR and azoxystrobin removal by different methods, including biodegradation and dielectric barrier discharges, and gas–liquid discharges. The removal rates of these methods ranged from 69% to 100%, and the treatment time ranged from 5 min to 72 h. In contrast, NPG-LD (in this work) and other ionizing treatment techniques have high removal efficiency in a short treatment time.

$$O_2 + e \rightarrow 2O + e \tag{5}$$

$$N_2 + e \rightarrow 2N + e \tag{6}$$

$$O + N \rightarrow NO \tag{7}$$

$$O + NO \rightarrow NO_2 \tag{8}$$

$$2NO_2 + H_2O \rightarrow NO_2^- + NO_3^- + 2H^+ \tag{9}$$

Table 1. Briefly compare the removal efficiency of different methods to remove Strobilurin fungicide.

Method	Concentration (mg/L)	Pollutant	Treatment Time	Applied Voltage (kV)	Remediation Efficiency (%)
Microbial/Fenton [37]	30	PYR	24/72 h	-	100
Photocatalysis/H₂O₂ [38]	0.5	PYR	12 h	-	90
Gas–liquid plasma [24]	6	Azoxystrobin	9 min	10	98.9
Dielectric barrier discharge (DBD) [39]	1.7	Azoxystrobin	5 min	80	69
This study	20	PYR	10 min	28	100

(a)

(b)

(c)

Figure 4. Effect of pulse peak voltage on (**a**) PYR removal efficiency, (**b**) pseudo-first-order kinetics, and (**c**) energy efficiency (pulse repetition rate: 150 Hz; initial concentration: 20 mg/L).

Figure 4b and c shows that the reaction kinetics and energy efficiency of the removal PYR in water varied with the discharge treatment time at 20 kV, 24 kV, and 28 kV, respectively. As the pulse peak voltage increased, so did the kinetic constant. The degradation of PYR in the NPG-LD plasma system followed the pseudo-first-level kinetic model with kinetic constants of $0.140 \ \text{min}^{-1}$, $0.208 \ \text{min}^{-1}$, and $0.323 \ \text{min}^{-1}$. More reactive species were produced as more energy was injected into the reactor at a higher pulse peak voltage [40]. The ultraviolet intensity and stronger electric field of the discharge plasma increased with increasing pulse peak voltage, and the water molecules collided and dissociated to form more reactive species (OH, H_2O_2) [41]. Therefore, the increase in the physicochemical effects led to higher PYR removal efficiency and rate at higher pulsed voltages. As shown in Figure 4c, the energy efficiency of PYR degradation decreased correspondingly as the treatment time increased. With the increase in treatment time, the number of PYR molecules gradually decreases, and the number of intermediate products produced by PYR molecular degradation gradually increases. The probability of collision between active species produced by discharge plasma and intermediate products increases, and more active species are consumed due to the reaction with intermediate products. The energy used for PYR molecular degradation decreases, leading to a decline in energy efficiency. During the same processing time, the energy efficiency decreased as the pulse peak voltage increased. After 1 min of plasma treatment, the efficiency was 13.32 g/kWh at 20 kV, while that dropped to 9.71 g/kWh and 5.75 g/kWh at 24 kV and 28 kV, respectively. Under different pulse voltages, the proportion of energy used for the degradation of PYR in water is different. When the peak pulse voltage is 20 kV, most of the energy is used for generating active species to promote the degradation of PYR. However, under high voltage, in addition to generating active species, the excess energy of discharge energy promotes the generation of NO_X and impedes the formation mechanism of reactive oxygen (ROS). NO_X competes with PYR molecules to consume ROS, electrons, etc. Therefore, the energy utilization rate of PYR degradation did not increase with the increase in voltage.

3.3. The Optical Emission Spectra of NPG-LD

Figure 5 displays the effect of applying different pulse peak voltages on the emission spectrum intensities of N_2 ($C^3\prod_u \rightarrow B^3\prod_g$), OH ($A^2\Sigma \rightarrow X^2\prod$), H$\alpha$, and O ($3p^5P \rightarrow 3s^5S^0$) during air discharge. The electrical parameters were fixed at a pulse repetition rate of 150 Hz and an airflow rate of 500 mL/min. The emission intensities of both OH ($A^2\Sigma \rightarrow X^2\prod$) and N_2 ($C^3\prod_u \rightarrow B^3\prod_g$) increased with increasing pulse peak voltage. The emission intensity of the active particles increased sharply when the pulse peak voltage increased from 22 kV to 26 kV. The pulse peak voltage increased the energy injected into the discharge region, increasing the number of generated high-energy electrons and the average electron energy. Therefore, the frequency and rate constant of the collision reaction between the electrons and gas atmosphere molecules in the bubble increased, and the number of N_2 (C), OH (A), and other active particles increased, resulting in an enhancement in OH ($A^2\Sigma \rightarrow X^2\prod$) and N_2 ($C^3\prod_u \rightarrow B^3\prod_g$) emission intensity.

3.4. Plasma Electron Density of NPG-LD

Due to the high emission intensity of the H$_\alpha$ line and the high sensitivity to Stark widening, the electron density (n_e) was determined by Stark broadening at 656.3 nm. The fullwidth at half maximum (FWHM) of the H$_\alpha$ was employed to calculate the ne by Equation (10) [42].

$$n_e = 10^{17} \left(\frac{\Delta\lambda_{Stark}}{0.549} \right)^{1.47135}, \tag{10}$$

where $\Delta\lambda_{Stark}$ represents the stark widening at FWHM, and n$_e$ is the electron density. The H$_\alpha$ is a vogit line type obtained from the convolution of Gaussian widening and Lorentz widening. Gaussian widening $\Delta\lambda_G$ is the result of Doppler widening $\Delta\lambda_D$ and instrument

widening $\Delta\lambda_L$ [43]. The instrument broadening $\Delta\lambda_L$ measured by the He-Ne laser (632.8 nm) was 0.02 nm.

$$\Delta\lambda_G = \sqrt{\Delta\lambda_D^2 + \Delta\lambda_L^2}, \tag{11}$$
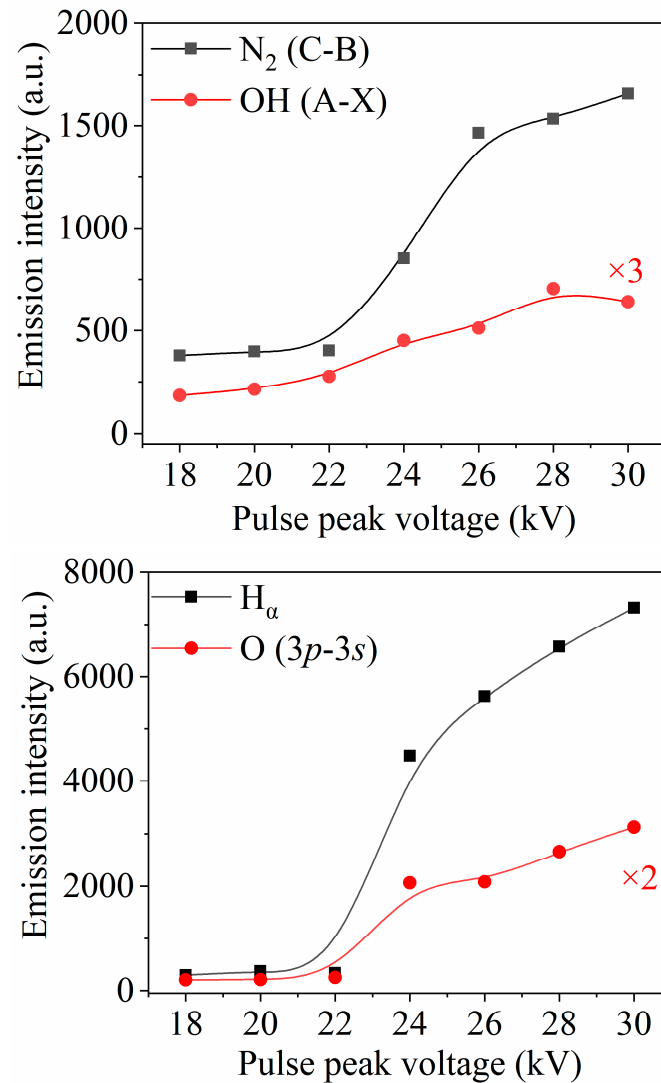
Figure 5. The emission intensities of OH (A$^2\Sigma \to$ X$^2\Pi$), N$_2$ (C$^3\Pi$u $\to$ B$^3\Pi$g), H$_\alpha$, and O (3p^{5}P $\to$ 3s^{5}S^0) varying the pulsed voltage.

The Doppler widening ($\Delta\lambda_G$) was calculated with Equation (12) [33].

$$\Delta\lambda_D = 7.162 \times 10^{-7} \, \lambda_0 \, T_g^{0.5}, \tag{12}$$

where λ_0 is the center wavelength, and T_g is the gas temperature. The van der Waals broadening $\Delta\lambda_v$ was calculated by Equation (13) [44].

$$\Delta\lambda_V = 8.18 \times 10^{-26} \, \lambda_0^2 \, T_g^{\frac{3}{10}} \left(\overline{R^2}\right)^{\frac{2}{5}} N \sum_i \frac{\alpha_i^{\frac{2}{5}} \chi_i}{\mu_i^{\frac{3}{10}}}, \tag{13}$$

$$\Delta\lambda_V = \frac{5.195}{T_g^{\frac{3}{10}}}, \tag{14}$$

where $\overline{R}^2$ indicates the difference between the values of the square radius of the emitting atom in the upper and lower levels, N is the background gas molecule number density, μ refers to the reduced mass (kg), α is the polarizability of the background gas molecule, and χ represents the fraction of the background gas molecule. All parameters were substituted into Equation (13). The van der Waals broadening of the H_α in an atmospheric pressure air discharge of Equation (14).

According to the Stark broadening method, the ne was calculated to be approximately 7.14×10^{17} cm^{-3} under the conditions of a 24 kV pulse peak voltage and a 500 mL/min gas flow rate. The electron density increased the voltage increased, as listed in Table 2. The comparison of the simulated and experimental H_α line is shown in Figure 6.

Table 2. The values of van der Waals broadening, Gaussian broadening, and Stark broadening of the H_α line.

Pulsed Voltage (kV)	$\Delta\lambda_G$ (nm)	$\Delta\lambda_V$ (nm)	$\Delta\lambda_{Stark}$ (nm)	Electron Density (10^{17} cm^{-3})
20	0.0224	0.070	0.3035	0.418
22	0.0225	0.069	0.3285	0.470
24	0.0225	0.069	2.0885	7.141
26	0.0225	0.069	2.2325	7.877
28	0.0225	0.067	2.3785	8.647
30	0.0225	0.068	2.4885	9.242
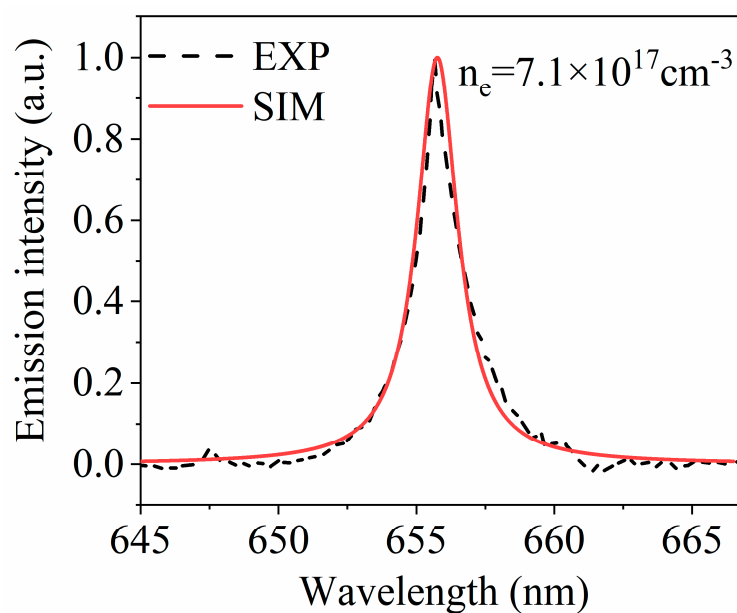
Figure 6. Comparison between the experimental and simulated results spectra of Hα for calculating electron density.

3.5. The Degradation Mechanism and Pathways of PYR

Intermediates degraded by PYR during plasma treatment were identified using HPLC-MS/MS, as shown in Figure 7. PYR was $m/z = 388$, and nine primary intermediates were detected. The possible molecular structures of these intermediates are provided in Table 3.
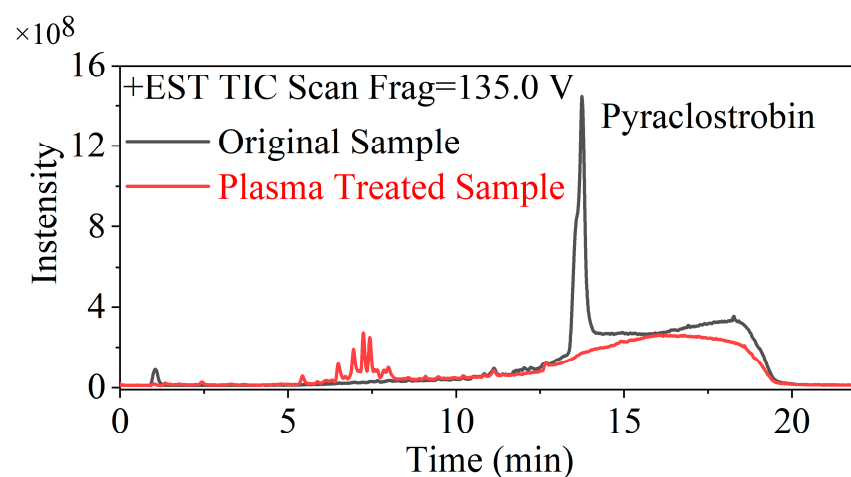
Figure 7. The chromatogram before and after plasma treatment was obtained by HPLC-MS/MS.

Table 3. Mass spectra data and structures of identified intermediates by HPLC-MS/MS for pyraclostrobin.
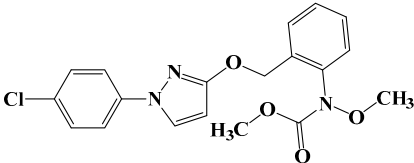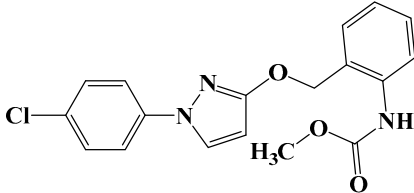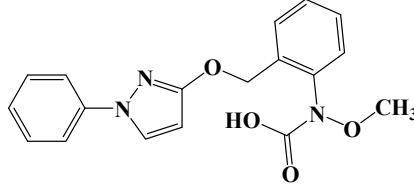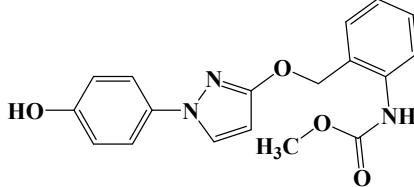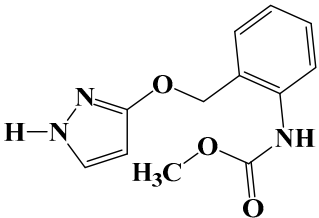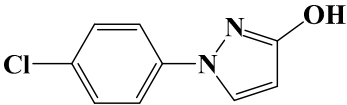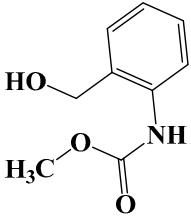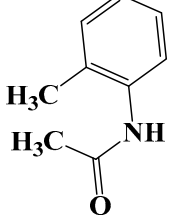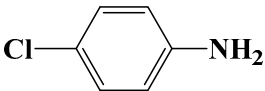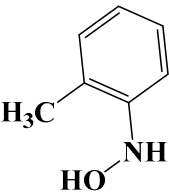
Structure	Retention Time (min)	*m/z*	Intensity
	13.749	388.2	388.2 (100) 194.2 (43.7) 163.2 (21.85) 356.2 (11.04)
	3.023	356.2	141.2 (100) 356.2 (90.95) 224.2 (78.29) 194.2 (72.9) 252.2 (61.4)
	5.427	340.4	340.4 (100) 341.4 (20.28) 362.3 (5.23)
	7.241	340.4	340.4 (100) 114.2 (4.76)

Table 3. *Cont.*

Structure	Retention Time (min)	*m/z*	Intensity
	9.622	246.4	141.2 (100) 246.4 (62.72) 123.2 (34.95) 275.2 (25.75)
	13.741	194.2	388.2 (100) 194.2 (42.82) 163.2 (22.12)
	1.482	181.1	181.1 (100) 123.2 (72.81) 141.2 (68.59) 194.1 (45.23)
	14.89	149.1	149.1 (100) 338.5 (34.96) 141.2 (14.4) 279 (12.12)
	8.012	127.1	99.1 (100) 183.2 (63.84) 155.2 (46.77) 127.1 (41.29)
	1.421	123.2	123.2 (100) 141.2 (28.04) 224.2 (21.04)

The prominent degradation locations of PYR were further explored. The geometry of the PYR was optimized using a Gaussian program, and the energies of some bonds were calculated, as shown in Figure 8. The bond energy of the PYR molecule was calculated by fitting the structure of the PYR molecule. The degradation of PYR was mainly realized by plasma in three ways. The average energy of electrons reached 0–20 eV by accelerating in a stronger electric field [5,45], which can break the chemical bonds of the pesticide molecules to form new bones. The inelastic collision between the gas/water molecules and high-energy electrons produced a large number of active species, such as O, H_α, OH, H_2O_2, O_3, etc., which effectively degraded pollutant molecules. Meanwhile, the UV radiation produced by the plasma discharge process photodegraded pesticides [46].
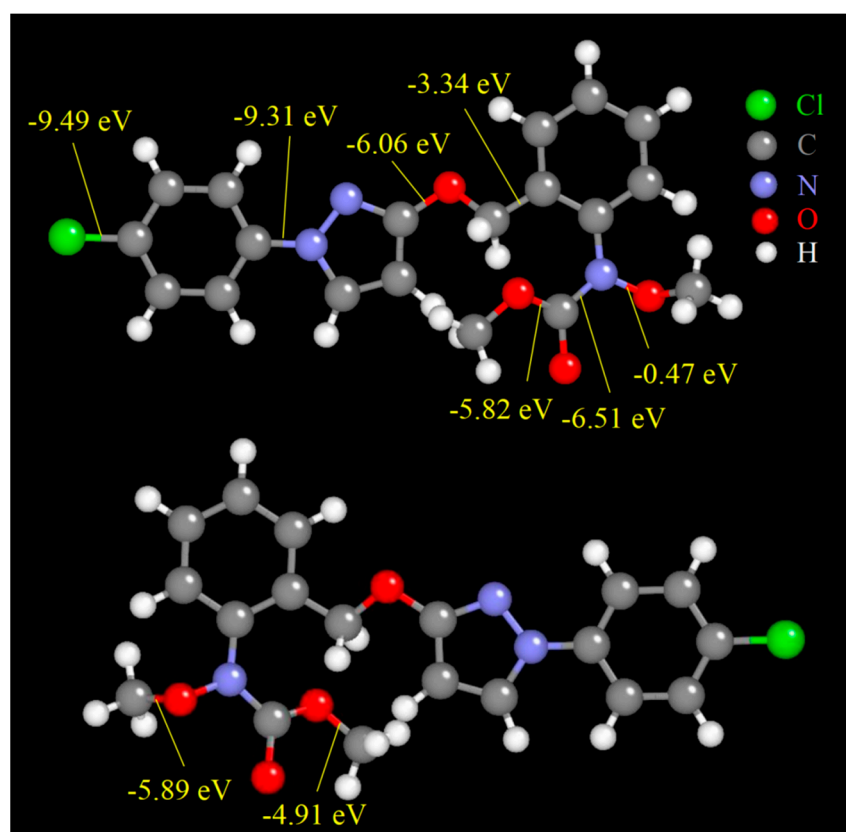
Figure 8. Optimized geometry and bonding of PYR.

The possible degradation pathways of PYR were obtained by combining the species and content of reactive species, electron density calculation, molecular structure optimization, bond energy calculation, HPLC-MS/MS analysis, and previous literature, as shown in Figure 9.
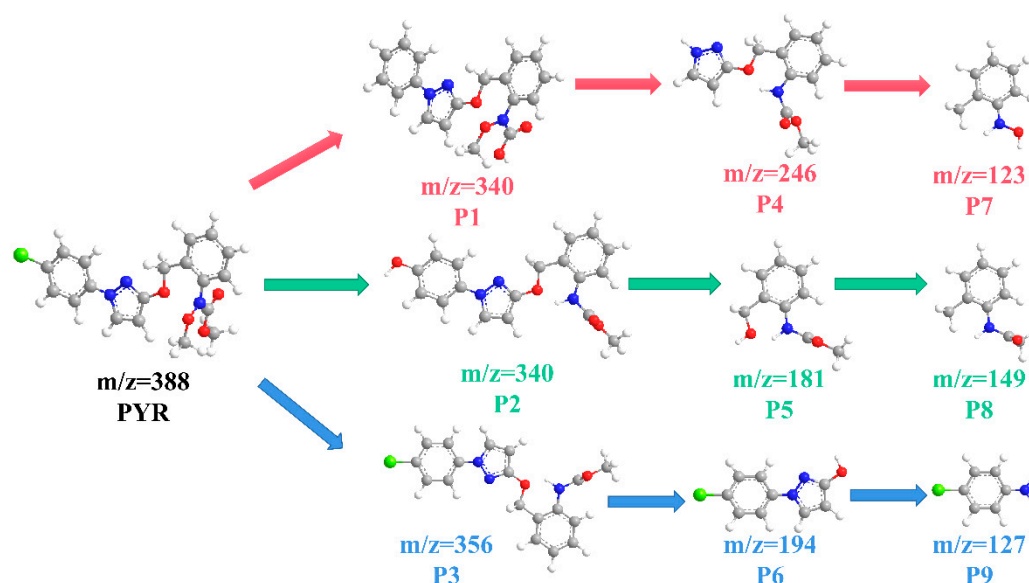

Figure 9. Possible degradation pathways of PYR in the NPG-LD system.

Pathway I: Fragments with m/z = 340 were obtained by removing by PYR side group Cl. After the five-membered ring continued to remove the benzene ring, the other side of the hydroxyl group H was replaced by methyl, and the ether bond was broken to obtain the

fragment molecules with $m/z = 246$. Finally, the ether bond broke, the analogous ring was removed, and the hydrolysis reaction ester bond was broken on the other side to obtain products with $m/z = 123$.

Pathway II: PYR side group Cl was substituted by OH, and the ether bond at N was broken to obtain a product with $m/z = 340$. The ether bond broke the oxygen right five-membered ring to receive a product with $m/z = 181$. The hydroxyl group was substituted by H, and the ether bond was utterly broken to form a methyl group, giving the product $m/z = 149$.

Pathway III: In this pathway, the ether bond at N was utterly broken, forming a product with $m/z = 356$. The ether bond linked by the latter five-membered ring was broken, and the products were divided into a five-membered ring part with $m/z = 194$ and a later five-membered ring. The pendant five-membered ring group of the chlorobenzene ring was changed to an amino group, generating a product with $m/z = 127$.

All the intermediates generated are further oxidized and decomposed by molecular bond-breaking reaction and finally mineralized into non-toxic and harmless Cl^-, NO_3^-, CO_2, and H_2O.

3.6. DFT Calculations and Ecotoxicity Analysis

According to the structural characteristics of the PYR molecule and the interaction between the high-energy electrons and active species on pesticide molecules, the Gibbs free energies of each intermediate were calculated, and the energy barriers of the above degradation paths were obtained, as shown in Figure 10. All three degradation pathways are exothermic, showing thermodynamically feasible, which also confirms the validity of the possible degradation pathways.
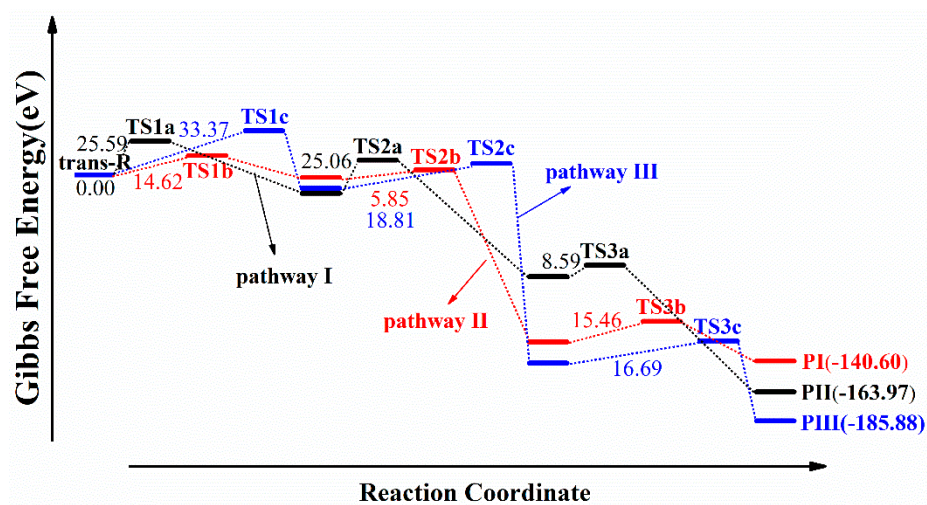

Figure 10. Profile of the potential energies of the intermediate products.

Ames mutagenicity and developmental toxicity of PYR and its intermediates were evaluated using the toxicity evaluation software tool (T.E.S.T.), as shown in Figure 11. Most intermediates exhibit low mutagenicity (Figure 11a). Some of the degradation intermediates showed relatively low developmental toxicity (Figure 11b), suggesting that the degradation process of PYR is accompanied by detoxification. Notably, the developmental toxicity of intermediates P4, P5, P8, and P2 was higher than that of PYR. However, their content is small and rapidly further mineralized into Cl^-, NO_3^-, CO_2, and H_2O. The results show that the gas–liquid discharge plasma degradation process can effectively degrade PYR and reduce its ecotoxicity. Gas–liquid discharge plasma wastewater treatment can be considered a green technology with great practical potential in eliminating PYR in water environments.
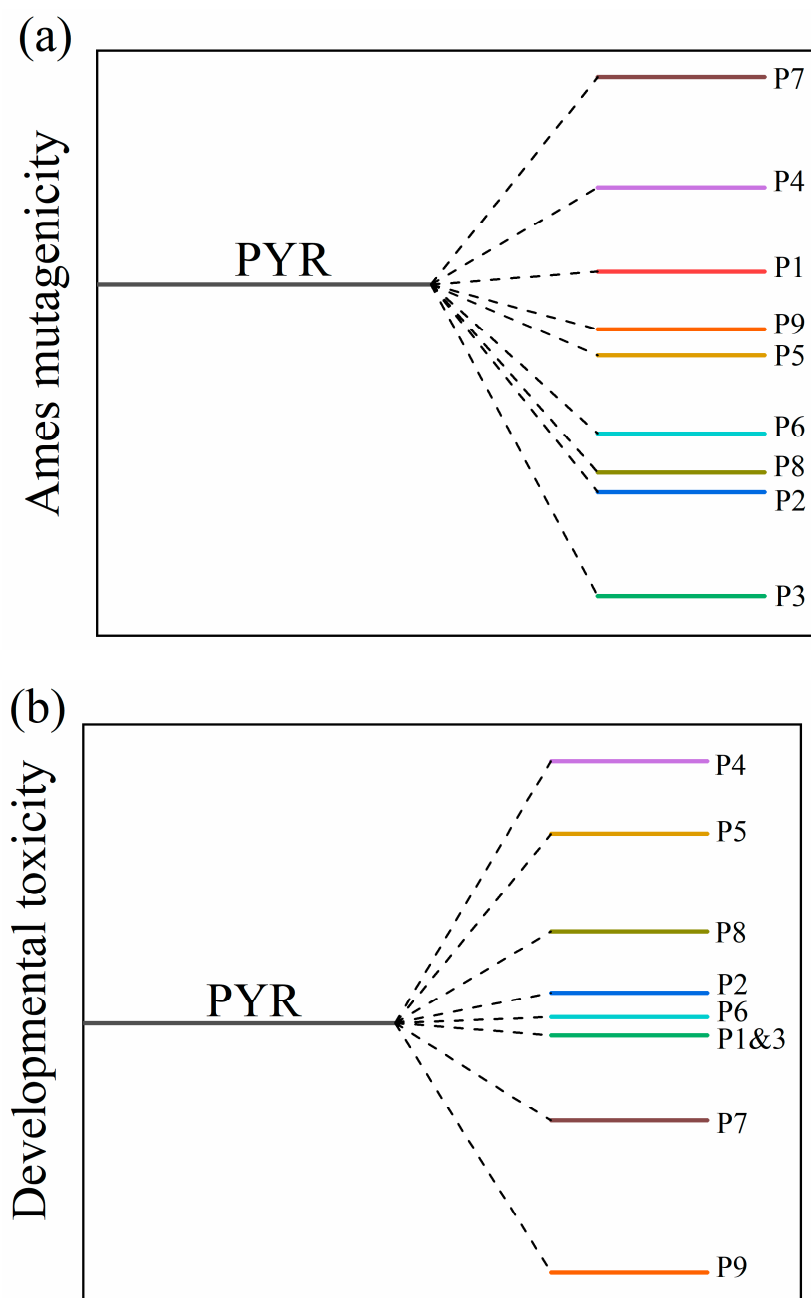
Figure 11. Ecotoxicity evaluation of PYR and intermediate products. (**a**) Ames mutagenicity, (**b**) Developmental toxicity.

4. Conclusions

In this paper, an air gas–liquid discharge plasma method was successfully developed for the efficient degradation of pyraclostrobin pesticide residues. The combination of liquid bubble discharge and liquid gas phase discharge generated a plasma with high electron density, which improved the formation of reactive species and enhanced the removal of organic pollutants. Below the pulse peak voltage of 24 kV, the electron density of 0.47×10^{17} cm^{-3}. When the voltage of the pulse exceeded 24 kV, the electron density was 7.1×10^{17} cm^{-3}. With the increase of pulse voltage, the reactive species (such as OH, O) increased significantly, and the electron density increased rapidly. The increase in voltage led to an increase in degradation kinetics and degradation efficiency, but the energy yield was the opposite. When the peak pulse voltage increases from 20 kV to 24 kV and 28 kV, the degradation rate increases from 79.7% to 90.4% and 100% after 10 min discharge

plasma treatments. Degradation rates increased from 0.140 min^{-1} to 0.208 min^{-1} and 0.323 min^{-1}. Energy yield decreased from 3.73 g/kWh to 3.08 g/kWh and 1.91 g/kWh. HPLC-MS/MS was used to analyze degradation byproducts, several intermediates were explored, and three possible degradation evolution processes were provided. The DFT was used to calculate the Gipps free energy of intermediates along each path to verify the degradation path's feasibility, and the intermediates' toxicity was analyzed. The toxicity of the intermediates was weak in the degradation of PYR by gas–liquid discharge plasma. The complete degradation of pyraclostrobin in water indicated that NPG-LD based low-temperature plasmas could be developed into a highly effective and environmentally friendly remediation technology for pesticide-contaminated water systems.

Data Availability Statement: The data that support the findings of this study are available from the corresponding author upon reasonable request.

References

1. Murugesan, P.; Monica, E.V.; Moses, J.A.; Anandharamakrishnan, C. Water decontamination using non-thermal plasma: Concepts, applications, and prospects. *J. Environ. Chem. Eng.* **2020**, *8*, 104377.
2. Yang, K.; Shen, H.W.; Liu, Y.Y.; Liu, Y.; Ge, P.J.; Yang, D.Z. Degradation of tiamulin by a packed bed dielectric barrier plasma combined with TiO_2 catalyst. *Plasma Sci. Technol.* **2022**, *24*, 095504. [CrossRef]
3. Tofa, T.S.; Ye, F.; Kunjali, K.L.; Dutta, J. Enhanced Visible Light Photodegradation of Microplastic Fragments with Plasmonic Platinum/Zinc Oxide Nanorod Photocatalysts. *Catalysts* **2019**, *9*, 819. [CrossRef]
4. Man, C.X.; Zhang, C.; Fang, H.Q.; Zhou, R.W.; Huang, B.D.; Xu, Y.Z.; Zhang, X.X.; Shao, T. Nanosecond-pulsed microbubble plasma reactor for plasma-activated water generation and bacterial inactivation. *Plasma Process. Polym.* **2022**, *19*, 2200004. [CrossRef]
5. Aggelopoulos, C.A. Recent advances of cold plasma technology for water and soil remediation: A critical review. *Chem. Eng. J.* **2022**, *428*, 131657. [CrossRef]
6. Liang, J.P.; Zhou, X.F.; Zhao, Z.L.; Yang, D.Z.; Wang, W.C. Degradation of trimethoprim in aqueous by persulfate activated with nanosecond pulsed gas-liquid discharge plasma. *J. Environ. Manag.* **2021**, *278 Pt 2*, 111539. [CrossRef]
7. Duan, L.J.; Rao, S.; Wang, D.X.; Zhang, K.F.; Cao, H.Y.; Liu, Z.Q.; Guo, Q.S.; Li, W.; Tao, J.Z.; Gao, Y. Understanding of TiO_2 catalysis mechanism in underwater pulsed discharge system: Charge carrier generation and interfacial charge-transfer processes. *Chemosphere* **2021**, *267*, 129249. [CrossRef] [PubMed]
8. Jungling, E.; Grosse, K.; von Keudell, A. Propagation of nanosecond plasmas in liquids-Streamer velocities and streamer lengths. *J. Vac. Sci. Technol. A* **2022**, *40*, 043003. [CrossRef]
9. Dong, G.; Chen, B.; Liu, B.; Hounjet, L.J.; Cao, Y.; Stoyanov, S.R.; Yang, M.; Zhang, B. Advanced oxidation processes in microreactors for water and wastewater treatment: Development, challenges, and opportunities. *Water Res.* **2022**, *211*, 118047. [CrossRef]
10. Wang, S.; Zhou, Z.; Zhou, R.; Fang, Z.; Cullen, P.J. Highly synergistic effect for tetracycline degradation by coupling a transient spark gas–liquid discharge with TiO2 photocatalysis. *Chem. Eng. J.* **2022**, *450*, 138409. [CrossRef]
11. Zhang, G.; Wang, T.; Zhou, J.; Guo, H.; Qu, G.; Guo, X.; Jia, H.; Zhu, L. Intrinsic mechanisms underlying the highly efficient removal of bacterial endotoxin and related risks in tailwater by dielectric barrier discharge plasma. *Water Res.* **2022**, *226*, 119214. [CrossRef]
12. Mohamed, Z.A.; Alamri, S.; Hashem, M. Endotoxin removal efficiency in conventional drinking water treatment plants, a case study in Egypt. *Water SA* **2022**, *48*, 180–186.
13. Rasuli, L.; Dehghani, M.H.; Aghaei, M.; Mahvi, A.H.; Mubarak, N.M.; Karri, R.R. Occurrence and fate of bacterial endotoxins in the environment (air, water, wastewater) and remediation technologies: An overview. *Chemosphere* **2022**, *303*, 135089. [CrossRef]

14. Ma, S.; Kim, K.; Chun, S.; Moon, S.Y.; Hong, Y. Plasma-assisted advanced oxidation process by a multi-hole dielectric barrier discharge in water and its application to wastewater treatment. *Chemosphere* **2020**, *243*, 125377. [CrossRef]

15. Wang, J.; Xing, C.; Xia, J.; Chen, H.; Zhang, J.; Yan, W. Degradation of carbendazim in aqueous solution by dielectric barrier discharge cold plasma: Identification and toxicity of degradation products. *Food Chem.* **2023**, *403*, 134329. [CrossRef]

16. Fang, C.; Wang, S.; Shao, C.; Liu, C.; Wu, Y.; Huang, Q. Study of detoxification of methyl parathion by dielectric barrier discharge (DBD) non-thermal plasma at gas-liquid interface: Mechanism and bio-toxicity evaluation. *Chemosphere* **2022**, *307*, 135620. [CrossRef]

17. Zhang, T.; Zhou, R.; Wang, P.; Mai-Prochnow, A.; McConchie, R.; Li, W.; Zhou, R.; Thompson, E.W.; Ostrikov, K.; Cullen, P.J. Degradation of cefixime antibiotic in water by atmospheric plasma bubbles: Performance, degradation pathways and toxicity evaluation. *Chem. Eng. J.* **2021**, *421*, 127730. [CrossRef]

18. Guo, H.; Wang, Y.W.; Liao, L.N.; Li, Z.; Pan, S.J.; Puyang, C.D.; Su, Y.Y.; Zhang, Y.; Wang, T.C.; Ren, J.Y.; et al. Review on remediation of organic-contaminated soil by discharge plasma: Plasma types, impact factors, plasma-assisted catalysis, and indexes for remediation. *Chem. Eng. J.* **2022**, *436*, 135239. [CrossRef]

19. Wang, R.; Li, Z.; Wang, H.; Chen, S.; Guo, P. High Efficiency Removal of Sulfur Mustard Surrogate by Cold Plasma Jet. *Plasma Chem. Plasma Process.* **2022**, *42*, 303–319. [CrossRef]

20. Tachibana, K.; Yasuoka, K. Understanding of chemical reactions induced by argon plasma in contact with sodium halide solutions: Importance of surface properties for plasma–liquid interactions. *J. Phys. D Appl. Phys.* **2020**, *53*, 125203. [CrossRef]

21. Oldham, T.; Chen, M.; Sharkey, S.; Parker, K.M.; Thimsen, E. Electrochemical characterization of the plasma-water interface. *J. Phys. D Appl. Phys.* **2020**, *53*, 165202. [CrossRef]

22. Zhou, R.; Zhou, R.; Alam, D.; Zhang, T.; Li, W.; Xia, Y.; Mai-Prochnow, A.; An, H.; Lovell, E.C.; Masood, H.; et al. Plasmacatalytic bubbles using CeO2 for organic pollutant degradation. *Chem. Eng. J.* **2021**, *403*, 126413. [CrossRef]

23. Zhou, X.F.; Liang, J.P.; Zhao, Z.L.; Yuan, H.; Qiao, J.J.; Xu, Q.N.; Wang, H.L.; Wang, W.C.; Yang, D.Z. Ultra-high synergetic intensity for humic acid removal by coupling bubble discharge with activated carbon. *J. Hazard. Mater.* **2021**, *403*, 123626. [CrossRef]

24. Chen, F.; Yang, D.; Yu, F.; Kun, Y.; Song, Y. The Effect of Mass Transfer Rate-Time in Bubbles on Removal of Azoxystrobin in Water by Micro-Sized Jet Array Discharge. *Catalysts* **2021**, *11*, 1169. [CrossRef]

25. Wang, S.; Liu, Y.W.; Zhou, R.W.; Liu, F.; Fang, Z.; Ostrikov, K.; Cullen, P.J. Microsecond pulse gas-liquid discharges in atmospheric nitrogen and oxygen: Discharge mode, stability, and plasma characteristics. *Plasma Process. Polym.* **2021**, *18*, 2000135. [CrossRef]

26. Liang, J.-P.; Zhao, Z.-L.; Zhou, X.-F.; Yang, D.-Z.; Yuan, H.; Wang, W.-C.; Qiao, J.-J. Comparison of gas phase discharge and gas-liquid discharge for water activation and methylene blue degradation. *Vacuum* **2020**, *181*, 109644. [CrossRef]

27. Myers, B.; Ranieri, P.; Smirnova, T.; Hewitt, P.; Peterson, D.; Herrera Quesada, M.; Lenker, E.; Stapelmann, K. Measuring plasma-generated·OH and O atoms in liquid using EPR spectroscopy and the non-selectivity of the HTA assay. *J. Phys. D Appl. Phys.* **2021**, *54*, 145202. [CrossRef]

28. Ning, W.J.; Lai, J.; Kruszelnicki, J.; Foster, J.E.; Dai, D.; Kushner, M.J. Propagation of positive discharges in an air bubble having an embedded water droplet. *Plasma Sources Sci. Technol.* **2021**, *30*, 015005. [CrossRef]

29. Liu, Y.; Song, J.-W.; Bao, J.; Shen, X.-J.; Li, C.-L.; Wang, X.; Shao, L.-X. Optimized Removal of Azo Dyes from Simulated Wastewater through Advanced Plasma Technique with Novel Reactor. *Water* **2022**, *14*, 3152. [CrossRef]

30. Cheng, J.; Fan, Y.; Pei, X.; Tian, D.; Liu, Z.; Yang, L.; Feng, E.; Ji, H.-F.; Chen, Q. An Energy Efficient Process for Degrading Perfluorooctanoic Acid (PFOA) Using Strip Fountain Dielectric Barrier Discharge Plasma. *Water* **2022**, *14*, 2420. [CrossRef]

31. Wu, L.; Xie, Q.; Lv, Y.; Wu, Z.; Liang, X.; Lu, M.; Nie, Y. Degradation of Methylene Blue via Dielectric Barrier Discharge Plasma Treatment. *Water* **2019**, *11*, 1818. [CrossRef]

32. Wang, S.; Liu, F.; Yang, D.-Z.; Wang, W.; Fang, Z. Characteristic study of a transient spark driven by a nanosecond pulse power in atmospheric nitrogen using a water cathode. *J. Appl. Phys.* **2019**, *125*, 043304. [CrossRef]

33. Zeng, L.R.; Shi, L.H.; Meng, X.G.; Xu, J.; Jia, G.F.; Gui, T.; Zhang, Y.P.; Hu, Y. Evaluation of photolysis and hydrolysis of pyraclostrobin in aqueous solutions and its degradation products in paddy water. *J. Environ. Sci. Health B* **2019**, *54*, 317–325. [CrossRef] [PubMed]

34. Sanito, R.C.; You, S.J.; Wang, Y.F. Degradation of contaminants in plasma technology: An overview. *J. Hazard. Mater.* **2022**, *424*, 127390. [CrossRef]

35. Šimečková, J.; Krčma, F.; Klofáč, D.; Dostál, L.; Kozáková, Z. Influence of Plasma-Activated Water on Physical and Physical–Chemical Soil Properties. *Water* **2020**, *12*, 2357. [CrossRef]

36. Liu, Y.; Liang, J.; Zhou, X.; Yuan, H.; Li, Y.; Chang, D.; Yang, K.; Yang, D. Degradation of persistent organic pollutants in soil by parallel tubes-array dielectric barrier discharge plasma cooperating with catalyst. *Chem. Eng. J.* **2022**, *437*, 135089. [CrossRef]

37. Zhao, H.; Kong, C.H. Elimination of pyraclostrobin by simultaneous microbial degradation coupled with the Fenton process in microbial fuel cells and the microbial community. *Bioresour Technol.* **2018**, *258*, 227–233. [CrossRef]

38. Skanes, B.; Ho, J.; Warriner, K.; Prosser, R.S. Degradation of boscalid, pyraclostrobin, fenbuconazole, and glyphosate residues by an advanced oxidative process utilizing ultraviolet light and hydrogen peroxide. *J. Photochem. Photobiol. A Chem.* **2021**, *418*, 113382. [CrossRef]

39. Misra, N.N.; Pankaj, S.K.; Walsh, T.; O'Regan, F.; Bourke, P.; Cullen, P.J. In-package nonthermal plasma degradation of pesticides on fresh produce. *J. Hazard. Mater.* **2014**, *271*, 33–40. [CrossRef] [PubMed]

40. Aggelopoulos, C.A.; Meropoulis, S.; Hatzisymeon, M.; Lada, Z.G.; Rassias, G. Degradation of antibiotic enrofloxacin in water by gas-liquid nsp-DBD plasma: Parametric analysis, effect of H_2O_2 and CaO_2 additives and exploration of degradation mechanisms. *Chem. Eng. J.* **2020**, *398*, 125622. [CrossRef]

41. Zhou, X.F.; Zhao, Z.L.; Liang, J.P.; Yuan, H.; Wang, W.C.; Yang, D.Z. Measurement of reactive species in different solutions of bubble discharge with varying O_2/N_2 proportion in Ar: Analysis of reaction pathways. *Plasma Process. Polym.* **2019**, *16*, e1900001. [CrossRef]

42. Szulc, M.; Forster, G.; Marques-Lopez, J.-L.; Schein, J. Influence of Pulse Amplitude and Frequency on Plasma Properties of a Pulsed Low-Current High-Voltage Discharge Operated at Atmospheric Pressure. *Appl. Sci.* **2022**, *12*, 6580. [CrossRef]

43. Yuan, H.; Yang, D.-Z.; Li, X.; Zhang, L.; Zhou, X.-F.; Wang, W.-C.; Xu, Y. A pulsed electrolyte cathode discharge used for metal element analysis by atomic emission spectrometry. *Phys. Plasmas* **2019**, *26*, 053505. [CrossRef]

44. Li, S.; Liu, Y.; Yuan, H.; Liang, J.; Zhang, M.; Li, Y.; Yang, D. Generation of High-Density Pulsed Gas-Liquid Discharge Plasma Using Floating Electrode Configuration at Atmospheric Pressure. *Appl. Sci.* **2022**, *12*, 8895. [CrossRef]

45. Wang, H.; Xu, Q.; Zhou, X.; Liang, J.; Yuan, H.; Yang, D.; Wang, W. Highly efficient adsorptive removal of persistent organic pollutants using NPD-acid combined modified NaY zeolites. *Chem. Eng. J.* **2022**, *431*, 133858. [CrossRef]

46. Lagunas-Allué, L.; Martínez-Soria, M.-T.; Sanz-Asensio, J.; Salvador, A.; Ferronato, C.; Chovelon, J.M. Degradation intermediates and reaction pathway of pyraclostrobin with TiO2 photocatalysis. *Appl. Catal. B Environ.* **2012**, *115–116*, 285–293. [CrossRef]